Check for updates

h-BN/graphene van der Waals vertical heterostructure: a fully spin-polarized photocurrent generator

Xixi Tao,[a,b] Lei Zhang, [iD] *[c,d,e] Xiaohong Zheng, [iD] *[a,b,d] Hua Hao, [iD] [a] Xianlong Wang,[a,b] Lingling Song,[f] Zhi Zeng[a,b] and Hong Guo[d,g]

By constructing transport junctions using graphene-based van der Waals (vdW) heterostructures in which a zigzag-edged graphene nanoribbon (ZGNR) is sandwiched between two hexagonal boron-nitride sheets, we computationally demonstrate a new scheme for generating perfect spin-polarized quantum transport in ZGNRs by light irradiation. The mechanism lies in the lift of spin degeneracy of ZGNR induced by the stagger potential it receives from the BN sheets and the subsequent possibility of single spin excitation of electrons from the valence band to the conduction band by properly tuning the photon energy. This scheme is rather robust in that we always achieve desirable results irrespective of whether we decrease or increase the interlayer distance by applying compressive or tensile strain vertically to the sheets or shift the BN sheets in-plane relative to the graphene nanoribbons. More importantly, this scheme overcomes the long-standing difficulties in traditional ways of using solely electrical field or chemical modification for obtaining half-metallic transport in ZGNRs and thus paves a more feasible way for their application in spintronics.

1. Introduction

With the successful fabrication of graphene,[1] a hexagonal lattice of carbon atoms with single atom thickness, and the discovery of its many remarkable properties soon afterwards, intensive interest has arisen to investigate other 2D materials. Thus far, many new 2D members, such as hexagonal boron-nitride sheets,[2] transition metal dichalcogenides,[3] black phospherene,[4] borophene,[5] 2D SiS layers,[6] 2D silicon carbide (SiC),[7–9] and many others,[10–14] have been added to the 2D material family. Such 2D materials are considered very important building blocks for future nanoelectronic and optoelectronic devices due to their extraordinary electronic and optoelectronic properties, such as high electron mobility or appropriate band gaps. In parallel with the efforts on continuously discovering new 2D materials, another important research direction on 2D materials has just emerged, which focuses on vertical van der Waals (vdW) heterostructures constructed by stacking different 2D crystals on top of one another.[15–24] Since the vdW interaction that binds the stacked layers together is rather weak, the exceptional properties of each layer are well preserved without any degradation. As a matter of fact, the construction of vdW heterostructures has become a very important method for extending the versatility and functionality of 2D materials and finding ways to develop new functions by building heterostructures has attracted more and more interest in the field of 2D materials.[25,26]

It is well known that achieving large spin polarization is an important issue in spintronics and the ultimate goal is to attain fully spin polarized electron conduction in a material or a device. Magnetism is a prerequisite for spin transport. In this regard, among all the 2D materials, graphene is probably the best-known candidate: when cut into nanoribbons, the resulting edges with zigzag geometry configurations have intrinsic edge magnetism arising from localized edge states, unlike most other 2D materials, where magnetism can basically only be induced externally by introducing defects or embedding transition-metal atoms or by other means.[27–30] More importantly, quite a few schemes have been suggested to

[a]*Key Laboratory of Materials Physics, Institute of Solid State Physics, Chinese Academy of Sciences, Hefei 230031, China. E-mail: xhzheng@theory.issp.ac.cn*
[b]*University of Science and Technology of China, Hefei 230026, China*
[c]*State Key Laboratory of Quantum Optics and Quantum Optics Devices, Institute of Laser Spectroscopy, Shanxi University, Taiyuan 030006, China. E-mail: zhanglei@sxu.edu.cn*
[d]*Department of Physics, Center for the Physics of Materials, McGill University, Montreal, Quebec H3A 2T8, Canada*
[e]*Collaborative Innovation Center of Extreme Optics, Shanxi University, Taiyuan 030006, China*
[f]*School of Electronic Science and Applied Physics, Hefei University of Technology, Hefei 230009, China*
[g]*School of Physics and Energy, Shenzhen University, Shenzhen 518060, China*

achieve half-metallicity (a property with only one conducting spin channel) in a zigzag edged graphene nanoribbon (ZGNR), such as electrical field,[31] edge decoration,[32] and B–N co-doping.[33,34] These schemes can be divided into two categories: one by applying an electrical field and the other by chemical modification. However, it has been shown that the strength of the electrical field should be extremely high to achieve half-metallicity in ZGNR, which is almost unavailable in the laboratory.[35] Meanwhile, with chemical modification it is hard to precisely control the doping or adsorption sites and structural stability. More importantly, as pointed out in our previous work, chemical modification can lead to a dramatic decrease or even the disappearance of the energy difference between the antiferromagnetic (AFM) and ferromagnetic (FM) edge configurations, whereas the half-metallicity can only be obtained from the AFM ground state.[36] Thus, a finite temperature can easily turn the ZGNRs paramagnetic, which makes the half-metallicity practically unobservable. Consequently, alternative schemes avoiding the use of either an electrical field or chemical modification for achieving fully spin polarized transport with ZGNRs are greatly anticipated.

In this work, we propose to realize this goal using graphene-based vdW heterostructures. First, a vdW heterostructure h-BN/graphene(Gr)/h-BN is constructed by sandwiching a ZGNR between two hexagonal BN sheets with AA stacking. The stagger potential produced by the two BN sheets at their middle plane acts differently on two sublattices of the ZGNR so that the energies of the edge states with different spins shift oppositely. Thus, the spin degeneracy of the edge states is lifted and two different spin energy gaps $E_{g\uparrow}$ and $E_{g\downarrow}$ (with $E_{g\uparrow} < E_{g\downarrow}$) are obtained. Second, linearly polarized light is shed on the central region of a device. By properly tuning the photon energy, electrons with only one spin can be excited from the valence band to the conduction band. Thirdly, through applying a small positive bias in the vdW heterostructure that is smaller than the energy gap $E_{g\uparrow}$, the excited electrons in the conduction band can be driven to the right lead, which results in a fully spin polarized photocurrent. This scheme is rather robust in that we can always achieve desirable results irrespective of whether we decrease or increase the interlayer distance by applying compressive or tensile strain vertically to the sheets or shift the BN sheets in-plane relative to the graphene nanoribbon, although the magnitude of the current produced and the photon frequency range needed may vary. Thus, 100% spin polarized transport can always be achieved in graphene/h-BN vdW junctions combined with light irradiation.

2. Theoretical formalism and computational details

The vdW vertical heterostructure device is presented in Fig. 1(a), in which a ZGNR is sandwiched between two zigzag-edged boron-nitride nanoribbons (ZBNNRs). The transport direction is along the z axis and the width of each ribbon in the x direction contains 6 zigzag chains. Each C/B/N atom at
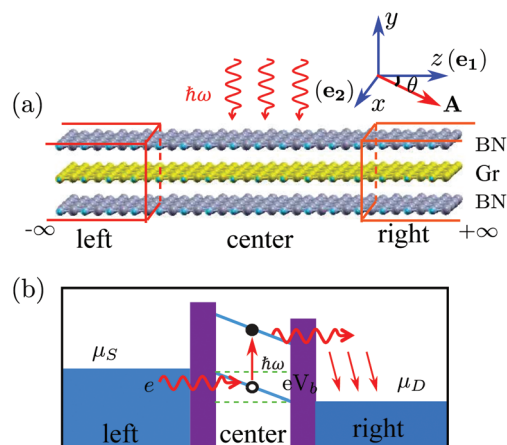

Fig. 1 (a) Schematic plot of the vdW vertical heterostructure with a 6-ZGNR (Gr) sandwiched between two 6-ZBNNRs (BN) by AA stacking and it is divided into the left lead, the right lead and the central region where the light impinges. The unit cells of the left and right leads are chosen to be the same, except for a case when discussing the polarization angle effect. The photon has energy $\hbar\omega$. The z axis is along the transport direction and the y axis is perpendicular to the 2D plane of the ribbons. The two vectors $\mathbf{e_1}$ and $\mathbf{e_2}$ defining the light propagation direction are parallel to the z and x axes respectively. 'BN' and 'Gr' label the BN sheet and graphene, respectively. $\mathbf{A}$ is the electromagnetic vector potential inside the xz plane. (b) The photocurrent generation process. A voltage $V_b < E_{g\uparrow}$ is applied between the left lead and the right lead to drive the excited electrons in the conduction band from the central region to the right lead.

the edge is saturated by a H atom. Due to the same hexagonal lattice structure and the very small lattice mismatch (<3%) of the BN sheet (bond length: 1.46 Å) and graphene (bond length: 1.42 Å), the lattice constants of BN ribbons are assumed to be the same as those of the ZGNR. The layers are stacked together by AA stacking which is more favorable in energy than AB stacking.[37] The distances between two adjacent layers are relaxed to be 3.22 Å. As shown in Fig. 1(a), the device is divided into three parts: the left lead, the right lead and the central region. The central region consists of 6 unit cells with a length of 14.76 Å including 252 atoms.

In our study, linearly polarized light is shone on the central region with the photon energy and the polarization direction being tunable. A small bias V_b is applied to create a potential drop so that the excited electrons in the conduction band can move unidirectionally from the central region to the right lead. Physically, the photocurrent generation process can be understood as follows (see Fig. 1(b)): the photon excites the valence electron to the conduction band in the central region. Driven by the potential drop, the excited electrons move to the right lead. At the same time, the electrons from the left lead move to the central region to fill the holes left by the previously excited electrons. This process goes on repeatedly and a continuous photocurrent is generated. If the applied bias voltage V_b is smaller than the band gap E_g, the electrical current will only have the photocurrent component, with no direct contribution from the bias.

The studied system can be described by the Hamiltonian $H = H_e + H_{e-ph}$, where H_e is the Hamiltonian of the two-probe system without the electron–photon interaction and $H_{e-ph} = \frac{e}{m}\mathbf{A} \cdot \mathbf{p}$ is the electron–photon interaction treated as a perturbation by the first Born approximation.[38] $\mathbf{A}$ is the electromagnetic vector potential and $\mathbf{p}$ is the momentum of the electron. As a matter of fact, the calculation of the photocurrent is a kind of post-analysis, which means that we will neglect the effect of H_{e-ph} during the self-consistent first-principles calculation and the Hamiltonian part of H_{e-ph} is treated as the perturbation after self-consistent Hamiltonian H_e is obtained. Then, the effective transmission function can be expressed in terms of Green's function[39]

$$T_{\alpha,s}(E) = \text{Tr}\{\Gamma_{\alpha,s}(E)[(1 - f_\alpha(E))G_s^<(E) + f_\alpha(E)G_s^>(E)]\}, \quad (1)$$

where α and s are the lead and spin index, respectively. For convenience, the spin index will be omitted from now on. Here, $\Gamma_\alpha = i(\Sigma_\alpha^r - \Sigma_\alpha^a)$ $(\alpha = L, R)$ is the linewidth function describing the coupling between the central region and both leads, with $\Sigma_\alpha^{r/a}$ being the self-energy of the semi-infinite α-th lead. f_α is the Fermi–Dirac distribution of the α-th electron reservoir. $G^{</>} = G_0^{</>} + G_{ph}^{</>}$ is the lesser/greater Green's function of the central region which takes account of the self-energies of both leads as well as the electron–photon interaction,

$$\begin{cases} G_0^{</>} = G_0^r\left(\Sigma_L^{</>} + \Sigma_R^{</>}\right)G_0^a \\ G_{ph}^{</>} = G_0^r\Sigma_{ph}^{</>}G_0^a \end{cases}. \quad (2)$$

It means that the effective transmission has two contributions, with the first one directly coming from the voltage and the other solely from photons. The retarded and advanced Green's functions in eqn (2) are defined as

$$G_0^r = [G_0^a]^\dagger = \frac{1}{E + i\eta - H_e - \Sigma_L^r - \Sigma_R^r} \quad (3)$$

without the electron–photon interaction. Meanwhile,

$$\Sigma_{ph}^> = NM^\dagger G_0^>(E + \hbar\omega)M \quad (4)$$

and

$$\Sigma_{ph}^< = NMG_0^<(E - \hbar\omega)M^\dagger \quad (5)$$

are the greater and lesser self-energies due to the electron–photon interaction where we only consider the adsorption process, with N being the number of photons.[39–41] In the atomic orbital basis $|n\rangle$, the matrix element

$$M_{nm} = \langle n|A_0\hat{\mathbf{e}} \cdot \mathbf{p}|m\rangle, \quad (6)$$

with A_0 being the amplitude of $\mathbf{A}$ which is independent of photon energy and incident direction but related to the photon flux, the number of photons and the specific material, while $\hat{\mathbf{e}}$ is the unit vector of $\mathbf{A}$ characterizing the polarization of light. For linearly polarized light,

$$\hat{\mathbf{e}} = \cos(\theta)\mathbf{e_1} + \sin(\theta)\mathbf{e_2}, \quad (7)$$

where $\mathbf{e_1} = (0, 0, 1)$ and $\mathbf{e_2} = (1, 0, 0)$ chosen in this work are two vertical unit vectors defining the plane in which $\mathbf{A}$ lies and $\mathbf{e_1} \times \mathbf{e_2}$ determines the propagation direction of light. For a specific device, A_0 together with N can be considered as constants.

The self-consistent calculations for H_e were performed combining density functional theory (DFT) with the nonequilibrium Green's function (NEGF) method for a quantum transport study,[42,43] as implemented in the Nanodcal package,[44] in which norm-conserving pseudopotentials and linear combinations of atomic orbitals as basis sets are adopted. The wave function is expanded with a double zeta polarized (DZP) basis set and the fineness of the real space grid is determined by an equivalent plane wave cutoff of 200 Ry. The exchange-correlation potential was treated at the level of generalized gradient approximation (GGA), using the functional of Perdew, Burke, Ernzerhof (PBE). The structure relaxation is performed over a smallest repeated unit cell by a conjugate gradient method until the residual force on each atom is less than 0.04 eV Å^{-1}. The convergence criterion of electronic self-consistent calculations is set as 1×10^{-4} *a.u.* for both the Hamiltonian matrix and the density matrix. The k-point sampling grid for both structure relaxation and the lead part of transport calculation is chosen as $1 \times 1 \times 100$.

The spin polarized current can be calculated by integrating the effective transmission function[39]

$$I_{\alpha,s}^{ph} = \frac{e}{h}\int T_{\alpha,s}(E)dE, \quad (8)$$

with h being the Plank's constant and e the electron charge.

3. Results and discussion

At the beginning, we calculate the band structures of the single ZGNR and the h-BN/Gr/h-BN structure (see Fig. 2(a) and (b)) to see the electronic structure difference between a pristine graphene nanoribbon and a vdW heterostructure. In the ground state, the two edges of the single ZGNR are anti-ferromagnetically (AFM) coupled. The magnetic moments of edge carbon atoms at the two edges are $0.29\mu_B$ and $-0.29\mu_B$, respectively. Note that the band structure of ZGNR is spin degenerate with a band gap of 0.63 eV (see Fig. 2(a)). Thus, for such an isolated ZGNR, photon irradiation with a certain photon energy $\hbar\omega > 0.63$ eV will excite electrons of both spins from the valence band to the conduction band and thus will generate a photocurrent with no spin polarization. In contrast, as shown in Fig. 2(b), the spin degeneracy is broken in the h-BN/Gr/h-BN vdW heterostructure. The band gap for spin up electrons is decreased to $E_{g\uparrow} = 0.28$ eV while that for spin down electrons is increased to $E_{g\downarrow} = 0.82$ eV. The energy gap at the X point changes from 0.95 eV to 0.50 eV and 1.15 eV for spin up and spin down, respectively. It is important to notice this for a later discussion of the photocurrent generation. Due to the existence of the BN sheets and the subsequent broken symmetry, the maximum magnetic moments of the edge carbon
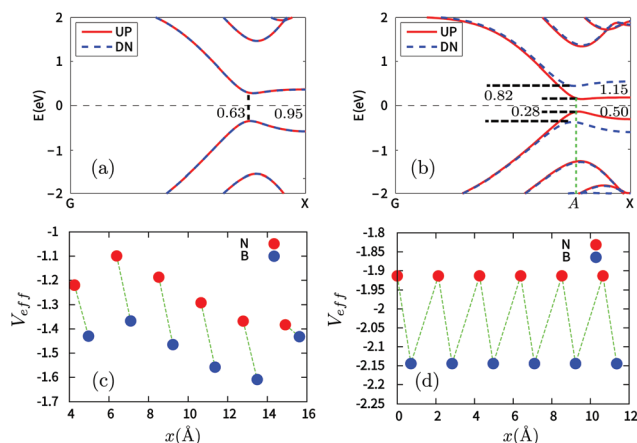
Fig. 2 The band structure of: (a) single layer ZGNR and (b) the *h*-BN/Gr/*h*-BN vdW vertical heterostructure. The numbers are the real energy gap values and those at the *X* point. The effective potential at the graphene plane produced by: (c) two BN nanoribbons and (d) two infinite BN layers. 'B' and 'N' indicate the C_B and C_N sites in graphene.

atoms decrease slightly and unequally to 0.28 and -0.26 μ_B, respectively.

Next, we will discuss the physics behind the spin degeneracy lift in the *h*-BN/Gr/*h*-BN system. There are two sublattices in both graphene and BN sheets. With AA stacking, if we view the system from top to bottom, the atoms of one sublattice in graphene overlap with the B atoms in the BN sheets and those of the other sublattice overlap with the N atoms. Thus, the two sublattices in graphene can be labelled as C_B and C_N, respectively (see Fig. 3). The existence of the BN sheets will produce a potential, which will influence the electronic structure of the

graphene nanoribbon. Since each C_B atom is between two B atoms and each C_N atom is between two N atoms, they will experience different local potentials produced by the BN sheets. To see the potential difference, we extracted the local potentials around each C_B and C_N atom by averaging around each site in a certain radius, which are shown in Fig. 2(c). The potential is obtained by artificially taking away the graphene layer with the positions of the BN sheets fixed. Clearly, the potential at each C_B site is much smaller than those at the neighboring C_N sites. Note that the potentials at the C_B sites (or C_N sites) are non-uniform due to the existence of boundaries and structure asymmetry. For infinite BN layers, the potential at each C_B site (or C_N) is exactly the same (see Fig. 2(d)).

Consequently, the BN sheets produce a stagger potential at the ZGNR plane, which is larger at the C_N sublattice and smaller at the C_B sublattice. Interestingly, we find that, in the ZGNR, the spin up edge states of the valence band are distributed only at the C_N sublattice and localized at the left edge (see Fig. 3(a)) while the spin down edge states of the valence band are only distributed at the C_B sublattice and localized at the right side (see Fig. 3(b)). Thus, the energy of the spin up edge state will be shifted up (close to the Fermi level) while that of the spin down edge state will be shifted down (away from the Fermi level). Likewise, in the conduction band, the spin up edge states are only distributed at the C_B sublattice (see Fig. 3(c)) while the spin down edge states are only distributed at the C_N sublattice (see Fig. 3(d)), which result in the energy of the spin up edge states shifting down (close to the Fermi level) and that of the spin down edge states shifting up (away from the Fermi level). Overall, the spin up edge states in both the valence and conduction bands shift close to the Fermi
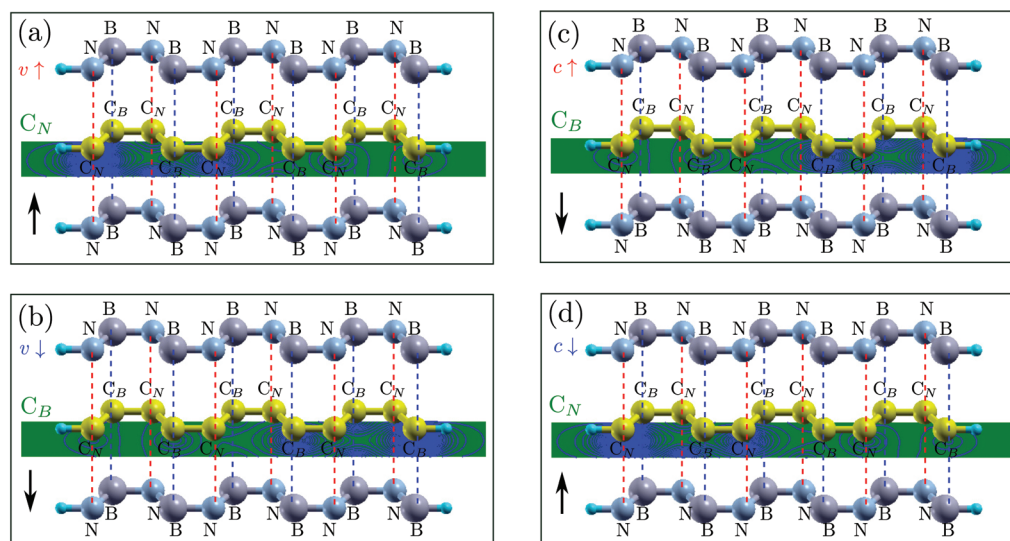

Fig. 3 The vdW structure and the edge states of the ZGNR for: (a) spin up in the valence band (v↑); (b) spin down in the valence band (v↓); (c) spin up in the conduction band (c↑); and (d) spin down in the conduction band (c↓). C_B and C_N indicate the carbon atoms in the two sublattices. In each panel, at the left border, the C_B or C_N in green indicates that the edge state is distributed at the C_B or C_N sublattice and the arrow at the down-left corner indicates the increase or the decrease of energy of the edge states. The edge states are obtained by calculation for a single ZGNR.

level while the spin down edge states move farther from it, resulting in the breaking of spin degeneracy (see Fig. 2(b)).

Having understood the spin splitting in the bandstructure of the h-BN/Gr/h-BN vdW vertical heterostructure, we now investigate the generation of a fully spin polarized photocurrent out of this vdW heterostructure. Generally speaking, a stable photocurrent can be directly generated by light irradiation without an external bias in two kinds of devices. One is based on the PN junction[41] and the other is a system with a lack of space inversion symmetry.[45] For other systems, a small bias should be applied to the device to create a potential drop along which the photon-excited electrons in the conduction band can move unidirectionally toward one electrode.[39] In our study, a linearly polarized light with photon energy $\hbar\omega$ is shed on the central region. The polarization direction (the direction of magnetic vector potential $\mathbf{A}$) in eqn (7) is chosen by taking $\mathbf{e_1}$ along the z axis, $\mathbf{e_2}$ along the x axis, and $\theta = 0°$ (see Fig. 1(a)). Considering the different spin band gaps (0.28 eV for spin up and 0.82 eV for spin down), we chose a bias voltage of 0.25 V, which will not produce a DC current directly between the two electrodes and the detected current in the device must be generated by photons. The photocurrent as a function of the photon energy $\hbar\omega$ is presented in Fig. 4(a). It is interesting to see that when the photon energy $\hbar\omega > 0.0$ and $\hbar\omega < 0.60$ eV, the spin up component of the photocurrent $I_{ph}^{\uparrow} \neq 0$ while the spin down component of the photocurrent $I_{ph}^{\downarrow} = 0$, producing a 100% spin polarized photocurrent.

In the following, we will further discuss three facts presented in Fig. 4(a): (1) the spin up photocurrent starts almost at $\hbar\omega = 0.0$ eV; (2) the spin down photocurrent starts when
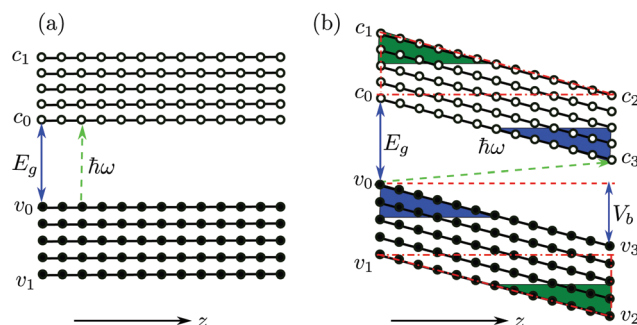

Fig. 5 A cartoon of the band profile of the edge states: (a) at equilibrium and (b) at a finite bias (V_b). The filled circles indicate the valence bands and the corresponding edge states while the empty circles indicate the conduction band and its corresponding edge states. In (b), $v_0 - v_3$ ($c_0 - c_3$) are four boundary points or states in the valence (conduction) band. V_b is the applied bias and E_g is the band gap. Green arrow indicates an excitation process between an edge state pair induced by a photon ($\hbar\omega$). z is along the transport direction.

$\hbar\omega > 0.55$ eV; and (3) the spin up photocurrent starts decreasing from 0.50 eV monotonously. To understand these features, we plot a cartoon figure for the tilting of the edge state band structure in the central region without and with the application of a bias (see Fig. 5). When $V_b = 0$, an electron can only be excited from the valence band to the conduction band when the photon energy $\hbar\omega \geq E_g$ (see Fig. 5(a)). However, when a bias voltage V_b is applied, the band structure gets tilted, that is, the energy of the states at the left side increases while that at the right side decreases (see Fig. 5(b)). The electrons at the
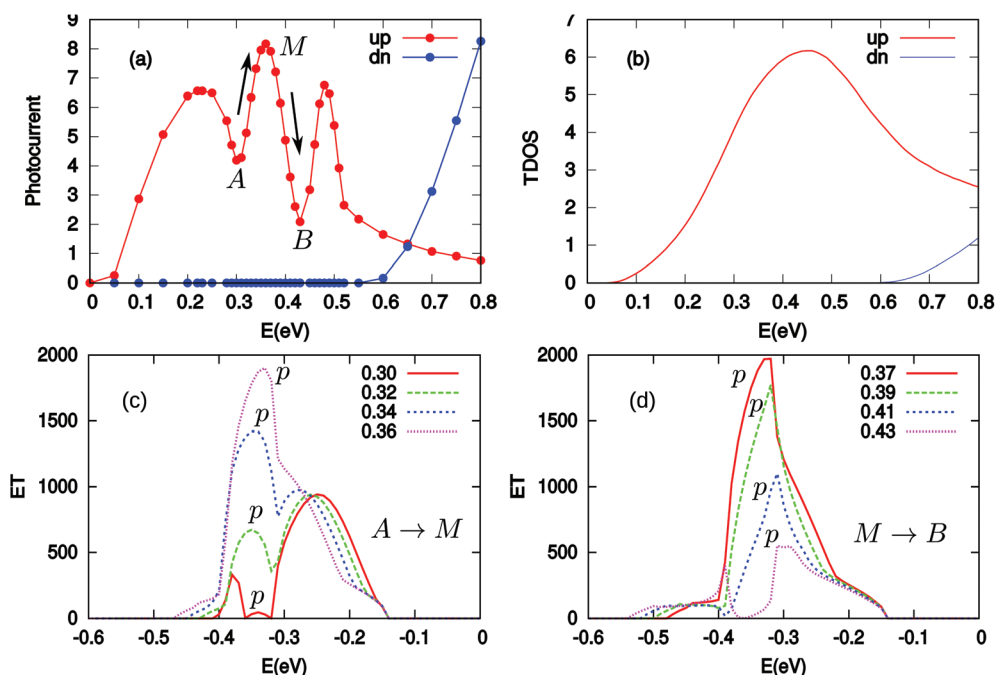

Fig. 4 (a) Two spin components of the photocurrent ($I_{\alpha,s}^{ph}$ with $\alpha = L$, $s = \uparrow$ and $\downarrow$) versus the photon energy ($E = \hbar\omega$) when a bias voltage of 0.25 V is applied in the system; (b) the transition density of states (TDOS) as a function of photon energy E; (c) and (d) the evolution of effective transmission (ET) function with the increase of photon energy for $A \to M$ and $M \to B$ stages, respectively.

up-left corner (see the blue triangle) in the valence band can be excited to the down-right corner (also see the blue triangle) of the conduction band by photons with much smaller energy. The minimum energy is determined by the excitation process from v_0 to c_3. For the spin up photocurrent, the starting energy $\hbar\omega = E_{g\uparrow} - V_b = 0.28 - 0.25 = 0.03$ eV. This is the reason that the spin up photocurrent starts almost at 0.0 eV when a bias of 0.25 V is applied. With the increase of $\hbar\omega$, more and more electrons in the blue triangle area (larger area) in the valence band will be excited to the blue triangle area in the conduction band (see Fig. 5(b)). Thus we see an increase in this region starting from 0 in the photocurrent. The same trend is observed for the spin down photocurrent, but the threshold energy will be $\hbar\omega = E_{g\downarrow} - V_b = 0.82 - 0.25 = 0.57$ eV. That is why the spin down photocurrent starts appearing when $\hbar\omega > 0.55$ eV. For the spin up component, since the energy difference between v_1 and c_1 is 0.50 eV (the band gap value at the X point in Fig. 2(b)), when $\hbar\omega = 0.50$ eV, all the electrons in the states above v_1 in the valence band cannot be excited into an available empty state in the conduction band; thus the excitation will be suppressed. At this time, all the states in the red dot-dashed triangle area crossing v_1 in the valence band can find an empty state in the red dot-dashed triangle area crossing c_2 in the conduction band to induce an excitation. With the increase of $\hbar\omega$, these two triangle areas for generating the photocurrent become smaller and smaller (see the green triangle area at down-right and up-left corners in Fig. 5(b)), which leads to the decrease of the photocurrent.

It is interesting to note the oscillations between 0.20 and 0.50 eV. There are three peaks (with the middle one labelled as "M") and two valleys (labelled as "A" and "B"). In order to understand these peaks and valleys, we calculated the transition density of states (TDOS). We use E_h^v to describe the energy of state h in the valence band and E_i^c to describe the energy of state i in the conduction band. When the band structure in the central region is tilted under a bias of 0.25 V, the energy of any state at different z (the position along the transport direction) will be $E_h^v(z_k) = E_h^v - \frac{z_k}{L_z} \times 0.25$ for the valence band and $E_i^c(z_j) = E_i^v - \frac{z_j}{L_z} \times 0.25$ for the conduction band, where z_j or z_k is the position along the z direction and L_z is the length of the central region. We may use a combination index hk to specify the state h in the valence band at positions k and ij to specify the state i in the conduction band at position j. A photon with energy $\hbar\omega_{hk,ij} = E_i^c(z_j) - E_h^v(z_k)$ can always find a pair of initial state hk and a final state ij between which it could excite an electron. The TDOS is defined as $n(E) = \Sigma_{hk,ij}\delta(E - \hbar\omega_{hk,ij})$. The TDOS including the contribution from both the edge states and the bulk states is shown in Fig. 4(b). For the spin up channel, the overall profile in the TDOS and the photocurrent are approximately the same. This demonstrates the great importance of TDOS in generating the photocurrent. However, we also have to note that the TDOS consists of only one large smooth peak while the photocurrent contains fine structures with three narrower peaks. This indicates that the TDOS is not the only factor determining the

photocurrent. Actually, the transition rate between different initial–final ($hk - ij$) state pairs may vary greatly. We calculated the effective transmission function as a function of valence electron energy corresponding to each photon energy studied in the photocurrent in Fig. 4(a). The effective transmission function is very important in understanding the photocurrent. On one hand, it directly reflects the transition rate at each valence electron energy under different photon energies. On the other hand, its integration leads to the photocurrent according to eqn (8). As an example, we will show the evolution of the effective transmission function with the photon energy increasing from valley A to peak M and then from peak M to valley B. They are shown in Fig. 4(c) and (d), respectively. We clearly see that for different photon energies, the effective transmission function and thus the transition rate are greatly different. We find for both the A → M stage and the M → B stage that the energy range for the excited valence electrons increases with the increase of photon energy. Meanwhile, in the A → M stage, there is a peak p increasing with the photon energy, which leads to the increase of the photocurrent. In contrast, in the M → B stage, the main peak p shrinks with photon energy, which leads to the decrease of the photocurrent.

The maximum energy range for the edge states determined by the energy difference between v_1 and c_2 is 0.75 eV. This can be understood as follows: from Fig. 2(b), we see that the band gap of spin up is 0.28 eV. This is the lowest photon energy that can be used to excite electrons when no bias is applied. However, also notice the gap of 0.5 eV at the X point. It is the largest photon energy that can be used to excite electrons from the edge states in the valence band to the edge states in the conduction band. However, when the band structure of the central region is tilted by a 0.25 V bias (see Fig. 5(b)), the largest photon energy for exciting electrons from the edge states in the valence band to the edge states in the conduction band, namely, from the state at v_2 to the state at c_1, will be 0.75 eV (0.50 + 0.25 = 0.75). If the photon energy is larger than 0.75 eV, no transition between edge states will occur. However, when $\hbar\omega > 0.75$ eV, the current can still be contributed by the transition between the bulk states located at the left part (G-A section) in the band structure shown in Fig. 2(b) and this is why we can still see a finite photocurrent when $\hbar\omega > 0.75$ eV for the spin up channel. It is worth mentioning that there is also a contribution from the bulk states in the 0.0–0.75 eV range.

From the discussion above, we see that the bias voltage plays an important role in the generation of photocurrent, and especially it directly affects the threshold of photon energy. It will be very interesting to know how it changes the magnitude of the photocurrent. For doing so, we fix the photon energy $\hbar\omega = E_{g,\uparrow} = 0.28$ eV and increase the bias voltage from 0.05 V to 0.25 V. The effective transmission function is presented in Fig. 6(a). It is seen that with the increase of the bias, the electrons in a larger energy range in the valence band can be excited to the conduction band and thus contribute to the photocurrent. This can be easily understood. When $V_b = 0.05$ V, the band structure in the central region is very slightly tilted, which can
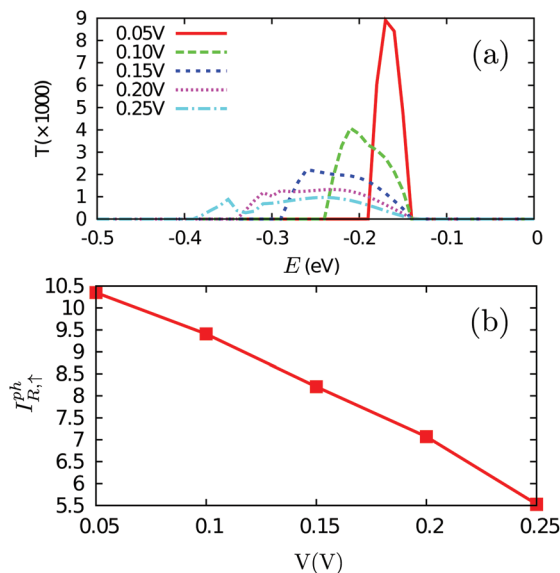
Fig. 6 The bias dependence of: (a) the effective transmission function and (b) the photocurrent in the right lead ('R'). The photon energy $\hbar\omega$ is fixed as 0.28 eV. In (a), E is the energy of the electrons excited in the valence bands. Only spin up is shown since the contribution of spin down is zero under these conditions.

still be approximated by Fig. 5(a). Only the electrons at the valence maximum through all the central region can be excited to the conduction minimum. With the increase of the bias, the band structure will be much more tilted; thus, electrons with lower energy can be excited. The width of the energy range of the excited electrons is exactly the magnitude of the applied bias. However, even though the energy range of the excited electrons is increased, the photocurrent is decreased (see Fig. 6(b)), which should arise from the decreased density of states at each energy and the decreased transition probability under a higher bias.

Proceeding further, we will study the effect of the polarization angle θ. Without the loss of generality, two cases are considered: (A) $V_b = 0.25$ V and $\hbar\omega = 0.20$ eV; (B) $V_b = 0.25$ V and $\hbar\omega = 0.10$ eV. The $I_\alpha^{ph}(\theta)$ as a function of θ is shown in Fig. 7 (see the curves labelled as 'A' and 'FA', 'B' and 'FB'). It is clear that both of them satisfy a cosine relationship with the period $T = \pi$. To understand it, with some derivation starting from eqn. (1) to (8), we have (with the spin index omitted):

$$I_\alpha^{ph}(\theta) = \sqrt{\left(\frac{a-b}{2}\right)^2 + c^2}\cos(2\theta + 2\phi_0) + \frac{a+b}{2} \quad (9)$$

where

$$\begin{cases} a = \frac{ie}{h}\int \mathrm{Tr}\left(\Gamma_\alpha\left[G_1^{<(ph)} + f_\alpha\left(G_1^{>(ph)} - G_1^{<(ph)}\right)\right]\right) \\ b = \frac{ie}{h}\int \mathrm{Tr}\left(\Gamma_\alpha\left[G_2^{<(ph)} + f_\alpha\left(G_2^{>(ph)} - G_2^{<(ph)}\right)\right]\right) \\ c = \frac{ie}{h}\int \mathrm{Tr}\left(\Gamma_\alpha\left[G_3^{<(ph)} + f_\alpha\left(G_3^{>(ph)} - G_3^{<(ph)}\right)\right]\right) \\ \phi_0 = \frac{1}{2}\arctan\left(\frac{2c}{a-b}\right) \end{cases} \quad (10)$$
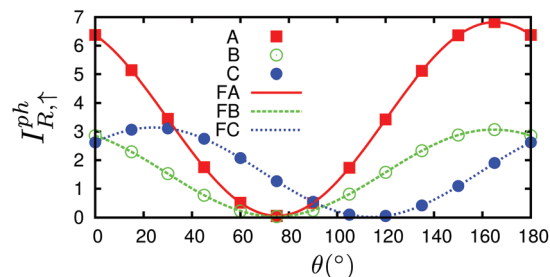

Fig. 7 The dependence of the photocurrent on polarization angle θ of three cases: (a) $V_b = 0.25$ V and $\hbar\omega = 0.20$ eV, labelled as 'A' and 'FA'; (b) $V_b = 0.25$ V and $\hbar\omega = 0.10$ eV, labelled as 'B' and 'FB'; (c) $V_b = 0.25$ V and $\hbar\omega = 0.10$ eV and the central region has a mirror symmetry, labelled as 'C' and 'FC'. 'A', 'B' and 'C' are the calculated data while 'FA', 'FB' and 'FC' are the corresponding fitted curves. Only spin up is nonzero and shown.

and

$$\begin{cases} G_1^{</>(ph)} = \sum_{\alpha,\beta=x,y,z} C_0 N G_0^r e_{1\alpha} p_\alpha G_0^{</>} e_{1\beta} p_\beta G_0^a \\ G_2^{</>(ph)} = \sum_{\alpha,\beta=x,y,z} C_0 N G_0^r e_{2\alpha} p_\alpha G_0^{</>} e_{2\beta} p_\beta G_0^a \\ G_3^{</>(ph)} = \sum_{\alpha,\beta=x,y,z} C_0 N G_0^r e_{1\alpha} p_\alpha G_0^{</>} e_{2\beta} p_\beta G_0^a \\ \qquad + \sum_{\alpha,\beta=x,y,z} C_0 N G_0^r e_{2\alpha} p_\alpha G_0^{</>} e_{1\beta} p_\beta G_0^a \end{cases} \quad (11)$$

where C_0 is a constant.[45] Therefore, the photocurrent $I_\alpha^{ph}(\theta)$ can be formulated into a simple function of $\cos(2\theta)$ with a period π.

It is seen that, the photocurrent is highly dependent on the polarization angle and can be switched on and off by tuning θ. The maximum/minimum photocurrent will be $\frac{a+b}{2} \pm \sqrt{\left(\frac{a-b}{2}\right)^2 + c^2}$. We see that $\theta = 0$, which means $\mathbf{A}//z$, does not correspond to a maximum photocurrent, but there is a phase shift of $2\phi_0$. By fitting, we get $I_\alpha^{ph} = 3.39 \times \cos(2\theta + 30.0) + 3.44$ for case (A) and $I_\alpha^{ph} = 1.52 \times \cos(2\theta + 30.0) + 1.55$ for case (B). Thus $\phi_0 \simeq 15.0°$ for these cases.

This phase shift is basically not caused/changed by the photon energy as seen, but by the asymmetry of the system, which can arise either from the structure asymmetry or from the bias. The bias induced asymmetry directly arises from the charge redistribution due to the bias and the subsequent asymmetrical potential profile. To prove that the bias can also cause the phase shift, we considered a third case (C) in which the central region is symmetrical by choosing the left and right leads with mirror symmetry. For $V_b = 0.25$ V and $\hbar\omega = 0.10$ eV, a phase shift is still seen from curve 'C' in Fig. 7. By fitting, we have $I_\alpha^{ph} = 1.56 \times \cos(2\theta - 48.0) + 1.58$; thus $\phi_0 \simeq -24.0°$. In a system with left–right symmetry studied by Xie *et al.*, namely, zigzag edged monolayer black phospherene nanoribbon doped with sulfur atoms, where both structural asymmetry and bias effect are absent and the photocurrent induced by linearly polarized light is totally caused by the photogalvanic effects, the phase shift is exactly zero.[45] In addition, from the three fitting expressions above we know
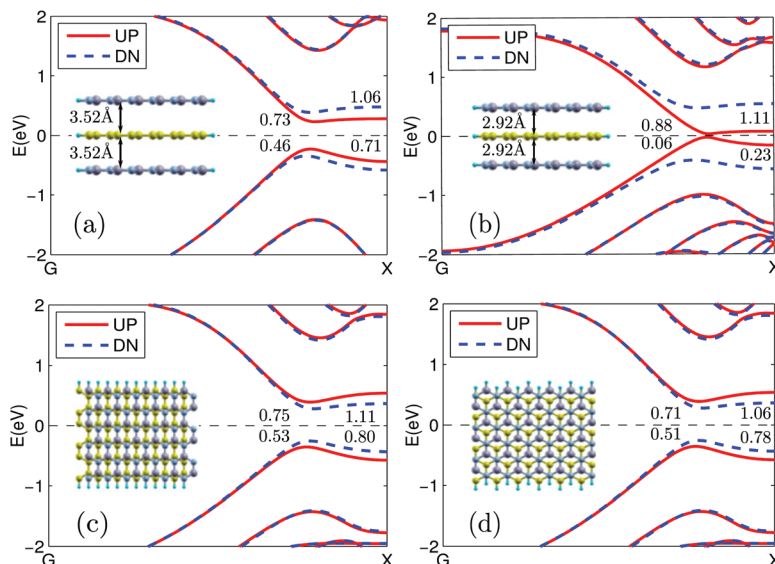
Fig. 8 The band structure for the cases in which: (a) the layer distance is increased by 0.30 Å; (b) the layer distance is decreased by 0.30 Å; (c) the ZGNR is shifted along the transport direction by half a unit cell and (d) the ZGNR is shifted along the *x* direction to make an AB stacking.

that the photocurrent I_α^{ph} will always be larger than zero, thus flowing to the right lead, due to the bias polarity applied.

Finally, to investigate the robustness of the full spin polarization of the photocurrent, we considered several factors that may lead to the changes of the geometry structures. We are mainly concerned with the effects of the vertical strain and the in-plane relative shift on the photocurrent. To be specific, we considered four cases: (1) an increase of the layer distance by 0.30 Å(+9.3%); (2) a decrease of the layer distance by 0.30 Å (−9.3%); (3) a shift of half a unit cell along the transport direction; and (4) AB stacking. We consider the first two cases since strain or pressure has become an important means for property and function tuning in the material or device design and we consider the last two cases since they may also appear in real situations although their structures are not the most stable. Especially, in practice, some degree of misalignment between the sheets would exist. The last two cases are typical ones which can give us information on effects of such misalignment. Since the spin polarization of the photocurrent is largely determined by the spin splitting of the band structure, for qualitative discussions, it is sufficient to analyze the band structure changes in these cases (see Fig. 8). It is seen that in all these cases, large spin splitting is always obtained. Especially, the change in the layer distance greatly affects the band structure. When it is increased by 0.30 Å, the band gap is increased to 0.46 eV and 0.73 eV for spin up and spin down, respectively (see Fig. 8(a)). Meanwhile, when the distance is decreased by 0.30 Å, the band gap for spin up is almost closed (0.06 eV) while that for spin down is increased to 0.88 Å (see Fig. 8(b)). This is because the smaller the layer distance, the larger the local potential difference between the C_B and C_N sublattices that will be produced, which increases the energy differences of the edge states of different spins. In the two cases of in-plane shift, which are two second most stable structures, besides the AA stacking that we

previously investigated, large spin splitting is still observed and they show almost equal band gaps for each spin (see Fig. 8(c) and (d), 0.53 and 0.51 eV for spin down while 0.75 and 0.71 eV for spin up). However, in case (3), after the shift, the C_B atoms are much closer to the N atoms than the B atoms while the C_N atoms are much closer to the B atoms, which leads to the increase of the band gap of spin up and the decrease of spin down, that is, spin down has a smaller band gap (see Fig. 8(c)). In the AB stacking shown in Fig. 8(d), the C_B atoms are right below (above) the N atoms while the C_N atoms are right below (above) the hexagon center; thus the spin up band gap is increased while the spin down band gap is decreased. Since the potential difference of the C_B and C_N sublattices in these two cases is smaller than the AA stacking, the spin splitting is also smaller. Therefore, a fully spin polarized photocurrent can always be achieved, although the required photon energy range and the produced photocurrent magnitude may be different.

4. Conclusion

In summary, we have proposed a *h*-BN/Gr/*h*-BN vdW heterostructure for generating a fully spin polarized photocurrent. Due to the stagger potential produced by the BN sheets, the two sublattices of the graphene nanoribbon experience different potentials imposed by the BN nanoribbons, which causes a shift of the energy of the edge states with different spins towards opposite directions. This results in the spin splitting of the band structure and makes single spin excitation possible by properly selecting the photon energy. Besides the most stable AA stacking structure, our systematic study of the other four cases changing the relative positions of the BN sheets to the graphene ribbons indicates that the fully spin polarized current can always be achieved, although the

photon energy range that can be used will be different. Note that, compared with the electrical or chemical ways for achieving fully spin polarized transport with graphene, the idea of the vertical Gr/*h*-BN vdW heterostructure is more practical since it can be easily fabricated by a lot of schemes, such as mechanical cleavage methods, layer-by-layer transfer techniques, co-segregation growth, temperature-triggered chemical switching growth or CVD growth.[19–21,46,47] In a word, by combining with photon irradiation, our study demonstrates the great importance and potential of 2D vdW heterostructures in spintronics, which should be taken into consideration in the design of spintronic devices based on 2D materials.

Conflicts of interest

There are no conflicts to declare.

Acknowledgements

References

1 K. S. Novoselov, A. K. Geim, S. Morozov, D. Jiang, Y. Zhang, S. Dubonos, I. Grigorieva and A. Firsov, *Science*, 2004, **306**, 666–669.

2 C. Zhi, Y. Bando, C. Tang, H. Kuwahara and D. Golberg, *Adv. Mater.*, 2009, **21**, 2889–2893.

3 K. Novoselov, D. Jiang, F. Schedin, T. Booth, V. Khotkevich, S. Morozov and A. Geim, *Proc. Natl. Acad. Sci. U. S. A.*, 2005, **102**, 10451–10453.

4 L. Li, Y. Yu, G. J. Ye, Q. Ge, X. Ou, H. Wu, D. Feng, X. H. Chen and Y. Zhang, *Nat. Nanotechnol.*, 2014, **9**, 372–377.

5 A. J. Mannix, X.-F. Zhou, B. Kiraly, J. D. Wood, D. Alducin, B. D. Myers, X. Liu, B. L. Fisher, U. Santiago, J. R. Guest, *et al.*, *Science*, 2015, **350**, 1513–1516.

6 J. Yang, Y. Zhang, W.-J. Yin, X. Gong, B. I. Yakobson and S.-H. Wei, *Nano Lett.*, 2016, **16**, 1110–1111.

7 M. N. Huda, Y. Yan and M. M. Al-Jassim, *Chem. Phys. Lett.*, 2009, **479**, 255–258.

8 X. Zheng, X. Chen, L. Zhang, L. Xiao, S. Jia, Z. Zeng and H. Guo, *2D Mater.*, 2017, **4**, 025013.

9 P. Jiang, X. Tao, H. Hao, L. Song, X. Zheng, L. Zhang and Z. Zeng, *2D Mater.*, 2017, **4**, 035001.

10 Y. Ma, Y. Dai, M. Guo, C. Niu, Y. Zhu and B. Huang, *ACS Nano*, 2012, **6**, 1695–1701.

11 D. C. Elias, R. R. Nair, T. M. G. Mohiuddin, S. V. Morozov, P. Blake, M. P. Halsall, A. C. Ferrari, D. W. Boukhvalov, M. I. Katsnelson, A. K. Geim, *et al.*, *Science*, 2009, **323**, 610–613.

12 D. Malko, C. Neiss, F. Viñes and A. Görling, *Phys. Rev. Lett.*, 2012, **108**, 086804.

13 D. D. Vaughn II, R. J. Patel, M. A. Hickner and R. E. Schaak, *J. Am. Chem. Soc.*, 2010, **132**, 15170–15172.

14 L.-D. Zhao, S.-H. Lo, Y. Zhang, H. Sun, G. Tan, C. Uher, C. Wolverton, V. P. Dravid and M. G. Kanatzidis, *Nature*, 2014, **508**, 373–377.

15 L. Samad, S. M. Bladow, Q. Ding, J. Zhuo, R. M. Jacobberger, M. S. Arnold and S. Jin, *ACS Nano*, 2016, **10**, 7039.

16 L. Ponomarenko, A. Geim, A. Zhukov, R. Jalil, S. Morozov, K. Novoselov, I. Grigorieva, E. Hill, V. Cheianov, V. Fal'Ko, *et al.*, *Nat. Phys.*, 2011, **7**, 958–961.

17 A. Azizi, S. Eichfeld, G. Geschwind, K. Zhang, B. Jiang, D. Mukherjee, L. Hossain, A. F. Piasecki, B. Kabius and J. A. Robinson, *ACS Nano*, 2015, **9**, 4882.

18 L. Britnell, R. Gorbachev, R. Jalil, B. Belle, F. Schedin, A. Mishchenko, T. Georgiou, M. Katsnelson, L. Eaves, S. Morozov, *et al.*, *Science*, 2012, **335**, 947–950.

19 C. R. Dean, A. F. Young, I. Meric, C. Lee, L. Wang, S. Sorgenfrei, K. Watanabe, T. Taniguchi, P. Kim, K. Shepard, *et al.*, *Nat. Nanotechnol.*, 2010, **5**, 722–726.

20 S. Haigh, A. Gholinia, R. Jalil, S. Romani, L. Britnell, D. Elias, K. Novoselov, L. Ponomarenko, A. Geim and R. Gorbachev, *Nat. Mater.*, 2012, **11**, 764–767.

21 Q. Li, M. Liu, Y. Zhang and Z. Liu, *Small*, 2016, **12**, 32–50.

22 T. Georgiou, R. Jalil, B. D. Belle, L. Britnell, R. V. Gorbachev, S. V. Morozov, Y.-J. Kim, A. Gholinia, S. J. Haigh, O. Makarovsky, *et al.*, *Nat. Nanotechnol.*, 2013, **8**, 100–103.

23 A. K. Geim and I. V. Grigorieva, *Nature*, 2013, **499**, 419–425.

24 Y. Liu, N. O. Weiss, X. Duan, H.-C. Cheng, Y. Huang and X. Duan, *Nat. Rev. Mater.*, 2016, **1**, 16042.

25 H. Sadeghi, S. Sangtarash and C. J. Lambert, *2D Mater.*, 2017, **4**, 015012.

26 J. Wong, D. Jariwala, G. Tagliabue, K. Tat, A. R. Davoyan, M. C. Sherrott and H. A. Atwater, *ACS Nano*, 2017, **11**, 7230.

27 O. V. Yazyev and L. Helm, *Phys. Rev. B: Condens. Matter Mater. Phys.*, 2007, **75**, 125408.

28 W. Hu and J. Yang, *J. Phys. Chem. C*, 2015, **119**, 20474–20480.

29 L. Seixas, A. Carvalho and A. H. Castro Neto, *Phys. Rev. B: Condens. Matter Mater. Phys.*, 2015, **91**, 155138.

30 A. Krasheninnikov, P. Lehtinen, A. S. Foster, P. Pyykkö and R. M. Nieminen, *Phys. Rev. Lett.*, 2009, **102**, 126807.

31 Y. W. Son, M. L. Cohen and S. G. Louie, *Nature*, 2006, **444**, 347.

32 E.-J. Kan, Z. Li, J. Yang and J. G. Hou, *J. Am. Chem. Soc.*, 2008, **130**, 4224.

33 S. Dutta, A. K. Manna and S. K. Pati, *Phys. Rev. Lett.*, 2009, **102**, 096601.

34 X. H. Zheng, X. L. Wang, T. A. Abtew and Z. Zeng, *J. Phys. Chem. C*, 2010, **114**, 4190.

35 E. J. Kan, Z. Li, J. Yang and J. G. Hou, *Appl. Phys. Lett.*, 2007, **91**, 243116.

36 X. H. Zheng, X. L. Wang, L. F. Huang, H. Hao, J. Lan and Z. Zeng, *Phys. Rev. B: Condens. Matter Mater. Phys.*, 2012, **86**, 081408(R).

37 J. Yu and W. Guo, *J. Phys. Chem. Lett.*, 2013, **4**, 951.

38 L. E. Henrickson, *J. Appl. Phys.*, 2002, **91**, 6273.

39 L. Zhang, K. Gong, J. Chen, L. Liu, Y. Zhu, D. Xiao and H. Guo, *Phys. Rev. B: Condens. Matter Mater. Phys.*, 2014, **90**, 195428.

40 L. E. Henrickson, *J. Appl. Phys.*, 2002, **91**, 6273–6281.

41 J. Chen, Y. Hu and H. Guo, *Phys. Rev. B: Condens. Matter Mater. Phys.*, 2012, **85**, 155441.

42 J. Taylor, H. Guo and J. Wang, *Phys. Rev. B: Condens. Matter Mater. Phys.*, 2001, **63**, 245407.

43 D. Waldron, P. Haney, B. Larade, A. MacDonald and H. Guo, *Phys. Rev. Lett.*, 2006, **96**, 166804.

44 For details of the NanoDcal quantum tranpsort package, see http://www.nanoacademic.ca.

45 Y. Xie, L. Zhang, Y. Zhu, L. Liu and H. Guo, *Nanotechnology*, 2015, **26**, 455202.

46 X. Song, J. Sun, Y. Qi, T. Gao, Y. Zhang and Z. Liu, *Adv. Energy Mater.*, 2016, **6**, 1600541.

47 Z. Liu, L. H. Tizei, Y. Sato, Y.-C. Lin, C.-H. Yeh, P.-W. Chiu, M. Terauchi, S. Iijima and K. Suenaga, *Small*, 2016, **12**, 252–259.